GEOLOGY

Subaerial volcanism broke mid-Proterozoic environmental stasis

Shuichang Zhang[1]*, Huajian Wang[1], Xiaomei Wang[1], Wang Zheng[2], Jihua Hao[3], Philip A. E. Pogge von Strandmann[4,5], Yuntao Ye[1,6], Miao Shi[2], Yuke Liu[1], Yitong Lyu[1]

The mid-Proterozoic, spanning 1.8 to 0.8 billion years ago, is recognized as a phase of marine anoxia, low marine primary productivity (MPP), and constrained eukaryotic biodiversity. However, emerging evidence suggesting intermittent environmental disturbances and concurrent eukaryotic evolution challenges the notion of a stagnant Earth during this era. We present a study detailing volcanic activity and its consequential impact on terrestrial weathering and MPP, elucidated through the examination of 1.4-billion-year-old tropical offshore sediments. Our investigation, leveraging precise mercury (Hg) and lithium (Li) isotopic analyses, reveals the introduction of fresh rock substrates by local volcanism. This geological event initiated a transformative process, shifting the initial regolith-dominated condition in tropical lowland to a regime of enhanced chemical weathering and denudation efficiency. Notably, the heightened influx of nutrient-rich volcanic derivatives, especially phosphorus, spurred MPP rates and heightened organic carbon burial. These factors emerge as potential drivers in breaking the long-term static state of the mid-Proterozoic.

INTRODUCTION

The narrative of planetary habitability and its intricate evolution is woven from the interplay of deep-seated tectonic forces, surface biogeochemical cycles, and life's transformative prowess (*1*). Against the backdrop of Earth's geological history, the mid-Proterozoic era [1.8 to 0.8 billion years (Ga) ago] heralded the emergence of single-celled eukaryotes, followed by the emergence and flourishing of multicellular eukaryotic life forms (*2*, *3*). However, this epoch's portrayal as the "boring billion" is rooted in the absence of widespread glaciations and iron (Fe) formations, persistent inorganic carbon isotope stasis around 0 per mil (‰) (*4*), and lower atmospheric oxygen content relative to subsequent epochs (*5*). This lull in environmental and biological evolution has been attributed to subdued orogenic activity (*6*). Concurrently, the coalescence of the Columbia supercontinent (~1.8 Ga) likely sustained its integrity for hundreds of millions of years (*7*). Diminished tectonic activity could have reduced the exposure of fresh rocks to continental weathering (termed soil shielding) (*6*), culminating in the reduced conveyance of essential nutrients such as phosphorus (P) and trace metals from continents to oceans (*8*, *9*). Given the importanceof these nutrients for marine primary productivity (MPP) (*10*), the mid-Proterozoic ocean endured a regime of sustained low MPP (*11*).

Nonetheless, recently increasing evidence challenges the narrative of a quiescent mid-Proterozoic Earth. The emergence of extensive organic-rich black shales from mid-Proterozoic epochs (*12*) signals sporadic surges in MPP. Geochemical probes of these shales and associated sedimentary strata unveil enrichments in redox-sensitive elements along with prominent isotopic fractionations (e.g., chromium, molybdenum, and uranium) (*13*–*15*). These indicators point to oscillations in atmospheric and oceanic oxygenation levels, which may potentially be linked to bio-diversification during the mid-Proterozoic. Although these trace elements and their corresponding environmental implications have been intensely studied and are relatively well characterized (*16*, *17*), the mechanisms driving the formation of their host black shales are not fully understood.

Prompted by these considerations, the role of large igneous provinces (LIPs) in punctuating the mid-Proterozoic status quo emerges (*12*, *18*), potentially instigating shifts in biogeochemical dynamics and evolutionary pathways. Precedent studies underscore the concurrence of notable climate and ecosystem shifts, including variation in the oceanic redox state and deposition of black shales, with LIP events (*1*). Geochronological and geological alignment strengthens the case for a temporal and causal nexus between LIPs and black shale deposition during 1.8 to 0.8 Ga (*12*). It is postulated that LIPs at ~1.57, ~1.38, and beyond ~1.1 Ga induced changes in the surface environments of the Earth system, potentially propelling the rise and evolution of eukaryotic life (*18*, *19*). However, the intricate web of causality remains enigmatic. Weathering of fresh volcanic rocks may enhance the release of pivotal nutrients such as P (*8*), sulfur (S) (*20*), and trace metals (*21*), ultimately contributing to the flourishing of MPP via riverine transport (*22*). This backdrop warrants an exploration of the symbiotic relationship between volcanic activity and environmental perturbations during the mid-Proterozoic.

Metal isotopes emerge as sensitive indicators of surface environmental evolution. Mercury (Hg), sourced predominantly from volcanic processes, is transported through global atmospheric circulation and subsequently stored within sedimentary rocks (*23*). The isotopic imprint of Hg showcases both mass-dependent fractionation (MDF; δ^{202}Hg) and mass-independent fractionations (MIFs; Δ^{199}Hg, Δ^{200}Hg, Δ^{201}Hg). Critically, MIF arises predominantly through aqueous or atmospheric photochemical interactions antecedent to Hg sedimentation, and its isotopic signals are resilient against postdepositional diagenetic alterations (*24*). Thus, mercury isotopes emerge as

[1]Key Laboratory of Petroleum Geochemistry, Research Institute of Petroleum Exploration and Development, China National Petroleum Corporation, Beijing 100083, China. [2]School of Earth System Science, Institute of Surface-Earth System Science, Tianjin University, Tianjin 300072, China. [3]Deep Space Exploration Laboratory/CAS Key Laboratory of Crust-Mantle Materials and Environments, University of Science and Technology of China, Hefei 230026, China. [4]LOGIC, Institute of Earth and Planetary Sciences, University College London and Birkbeck, University of London, Gower Street, London, WC1E 6BT, UK. [5]MIGHTY, Institute of Geosciences, Johannes Gutenberg University, 55122 Mainz, Germany. [6]Key Laboratory of Orogenic Belts and Crustal Evolution, School of Earth and Space Sciences, Peking University, Beijing 100871, China.
*Corresponding author. Email: sczhang@petrochina.com.cn

a cardinal tracer of Hg sources within sedimentary records. Lithium (Li), recognized for its high mobility, endows its content and isotopic composition (δ^7Li) with distinction as a proxy for weathering processes (*25*). The selective incorporation of ^{6}Li into secondary minerals formed during weathering produces ^{7}Li enrichment within river catchments and seawater, relative to average crustal values (*26*). Notably, the relationship between detrital δ^7Li and weathering intensity, expressed as the ratio of weathering rate to denudation rate (W/D), can adopt a negative (*27*) or "boomerang" (*28*, *29*) configuration. In the latter configuration, δ^7Li values are low at both low and high weathering intensity, and high at medium intensity (*28*). While Hg and Li isotopic proxies have heretofore been explored in isolation, the combined use of them has not been explored.

Within this context, our study delves into the 1.41- to 1.35-Ga Xiamaling Formation in North China. Imbued with high-precision age-constrained Hg, Li content, and isotopic data, alongside supplementary geochemical and mineralogical insights, our study delineates a narrative of local subaerial volcanic events preceding a LIP episode [1382 million years (Ma)] (*30*) that augmented continental weathering. The ensuing nutrient input propelled MPP and triggered the deposition of black shales. Our findings suggest that the influence of subaerial volcanism could have been pivotal in disrupting the prolonged stagnation of the mid-Proterozoic, thereby exerting a substantial impact on the evolution of Earth's surface environments.

The Xiamaling Formation characterized by siliciclastic rocks was established within a tropical gulf during the disintegration of the Columbia supercontinent (fig. S1). A lithological and geochemical tableau partitions the Xiamaling Formation into six units, with U6, U5, and U4 in the lower part composed of organic-lean sediments, while U3, U2, and U1 in the upper part are predominantly organic-rich black shales (*31*). In the Xiahuayuan section, multiple volcanic ash layers within U3 and U2 provide direct evidence of coeval volcanic activity (Fig. 1). Notably, the Isotope Dilution Thermal Ionization Mass Spectrometry (ID-TIMS) zircon U-Pb ages of the tuff layers (~211 m) within U2 (1384.4 ± 1.4 Ma) and the K-bentonite layer (262.4 m) within U3 (1392.2 ± 1.0 Ma) (*32*) synchronize U2 deposition with the 1382-Ma LIP event (Fig. 2 and fig. S2) (*30*), while U3 predates this LIP occurrence.

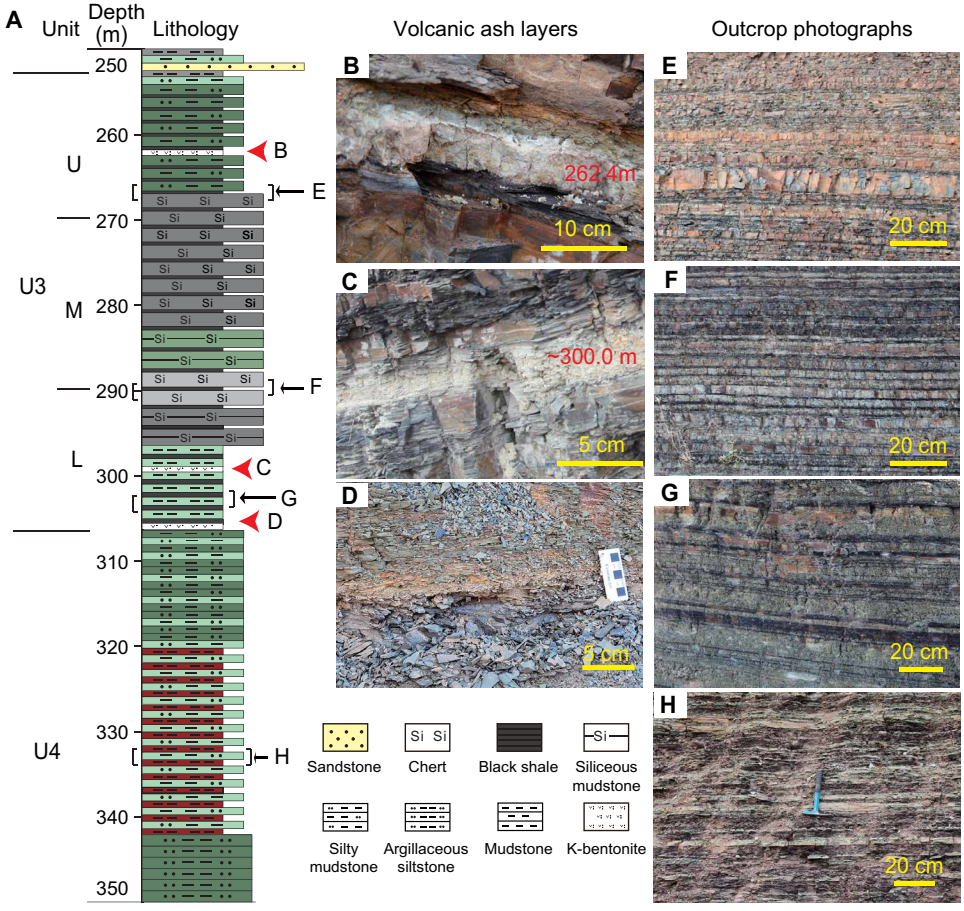

Fig. 1. Lithological column, volcanic ash layers, and outcrop photos of U4 and U3 sediments in the Xiahuayuan section of the Yanliao Basin in the North China Craton. Because of the lithological (**A**), mineralogical and geochemical evidence (see Results), U3 was proposed to be further divided into lower part (U3L, 307 to 290 m), middle part (U3M, 290 to 270 m), and upper part (U3U, 270 to 255 m). The zircon U-Pb age of the K-bentonite at 262.4 m (**B**) is 1392.2 ± 1.0 Ma (*32*). The ash layers in (**C** and **D**) are newly found without zircon U-Pb age. Outcrop images show the interbedding of black shale and gray chert and the interbedding of black shale and green siliceous mudstone in U3U (**E**), the interbedding of black shale and gray chert in U3M (**F**), the interbedding of black shale and green silty mudstone in U3L (**G**), as well as the interbedding of red mudstone and green silty mudstone in U4 (**H**). Depth locations of these outcrop photographs of (B) to (H) were marked in (A). Photograph credit: Huajian Wang, Research Institute of Petroleum Exploration and Development.

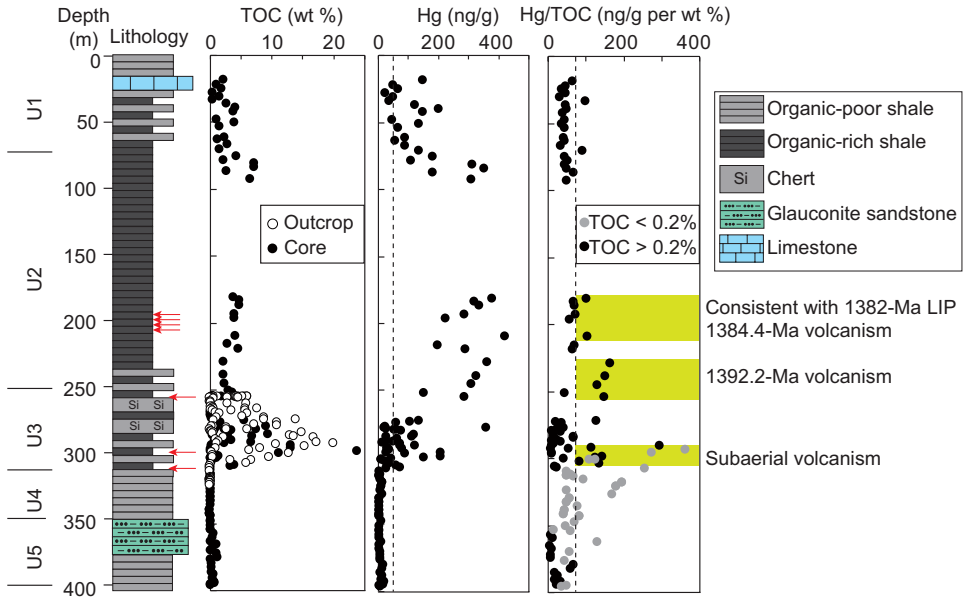

Fig. 2. Sedimentary TOC, mercury (Hg), and Hg/TOC values of the Xiamaling Formation. Red arrows represent volcanic ash layers. The dash lines in the Hg and Hg/total organic carbon (TOC) panels are Hg content (50 ng/g) of the upper crust (*33*) and the mean Hg/TOC value (71.9 ng/g per wt %) of the Phanerozoic sediments (*23*), respectively. The shadows in Hg/TOC panel represent depth ranges with Hg/TOC values over 71.9 ng/g per wt %, consistent with the appearance of volcanic ash layers.

Our focal point lies within the sedimentary strata of U4 and U3. Unit 4 is delineated by grayish-green siltstone at its extremities, with intermittent interstratifications of grayish-green argillaceous siltstone and purplish-red mudstone in the middle (Fig. 1A). Meanwhile, U3 is characterized by alternating layers of organic-rich black shales and organic-lean green mudstones or cherts (Fig. 1A). Intriguingly, U3 is also punctuated by at least three volcanic ash layers at depths of 262.4, 300.0, and 307.0 m (Fig. 1, B to D). Both U3 and U4 unveil rhythmic sequences of lithologic unit thicknesses, spanning centimeters to meters (Fig. 1, E to H), which are likely indicative of climatic alternations (*32*).

RESULTS

The sedimentary Hg content exhibits a distinctive two-stage pattern, ascending from the organic-lean U5 and U4 (7.2 ± 5.2 ng/g; means ± SD) to the organic-rich U3 (84.0 ± 76.9 ng/g) and U2 (286.1 ± 82.5 ng/g) (Fig. 2; refer to Materials and Methods for detailed analytical procedures). This trend is followed by a decline in U1 (90.4 ± 50.5 ng/g) (Fig. 2). The majority of organic-rich shales exhibit Hg levels surpassing the upper crustal value of 50 ng/g (*33*) and also the mean value of Phanerozoic sediments at 62.4 ng/g (*23*). However, when normalized to total organic carbon (TOC), most Hg/TOC ratios are lower than the mean value of Phanerozoic sediments, which is 71.9 ng/g per wt % (Fig. 2) (*23*). Intriguingly, elevated Hg/TOC ratios occur in the lower parts of U3 and U2 (U3L and U2L), coinciding with horizons where volcanic activity is evident due to the presence of ash layers (Fig. 2). The Hg/TOC ratios of U3L, containing volcanic ash layers, span from 6.0 to 294.2 ng/g per wt % with a mean value of 75.0 ± 81.2 ng/g per wt %, surpass that of the middle part of U3 (U3M) (33.0 ± 29.0 ng/g per wt %), which lacks identifiable ash layers (Fig. 3A and Table 1).

Transitioning from U4 to U3, the Hg isotopic compositions display opposing shifts in Hg-MDF (δ^{202}Hg) and Hg-MIFs (Δ^{199}Hg and Δ^{200}Hg) (Fig. 3A and Table 1). The δ^{202}Hg values show a positive shift, progressing from U4 (−1.54 ± 0.74‰) to U3 (−0.67 ± 0.30‰). Meanwhile, both Δ^{199}Hg and Δ^{200}Hg undergo a negative shift, transitioning from slightly positive values in U4 to near-zero values in U3. One-way analysis of variance (ANOVA) tests of δ^{202}Hg and Δ^{199}Hg values between U4 and U3L shows statistical significance ($P < 0.01$ for δ^{202}Hg and $P < 0.05$ for Δ^{199}Hg; figs. S3 and S4). For Δ^{200}Hg values, a slightly larger P value of 0.08 (fig. S3C) of the one-way ANOVA test between U4 and U3L is probably due to the low Δ^{200}Hg values (within ±0.04‰). Box plots of all Hg isotope values also show significantly more negative δ^{202}Hg, more positive Δ^{199}Hg, and slightly more positive Δ^{200}Hg in U4 than those in U3L (fig. S3).

In the context of sediment compositions, U4 sediments display relatively low Li/Al ratios (3.9 ± 1.4 μg/g per wt %), coupled with high δ^7Li values that decrease as the unit progresses upward (a negative shift from 2.35 to −1.03‰) (Fig. 3B and Table 1). In contrast, U3L sediments exhibit higher Li/Al ratios (6.3 ± 0.5 μg/g per wt %) and concurrently lower δ^7Li values (−1.31 ± 0.31‰) (Fig. 3B and Table 1). Between U4 and U3L, variations of both Li/Al ratios and δ^7Li values show statistical significance (ANOVA, $P < 0.001$; Fig. 3B and fig. S3). U3M sediments demonstrate slightly increased Li/Al ratios (8.0 ± 1.6 μg/g per wt %), alongside higher δ^7Li values, oscillating from −0.26 to 6.79‰ (mean value, 2.25 ± 2.33‰) in comparison to U3L (Fig. 3B and Table 1).

Assessing chemical weathering, the chemical index of alteration (CIA) values of U3L sediments (82.2 ± 0.8) are notably reduced, when compared to those of U4 (84.4 ± 1.0) and U3M (84.6 ± 1.1) sediments (Fig. 3B and Table 1; note that the correction of CIA can be found in fig. S5) (*34*, *35*). The zircon (Zr) weight content normalized to aluminium (Zr/Al) is widely recognized as a proxy for terrestrial erosion and riverine transport efficiency (*32*). It displays a

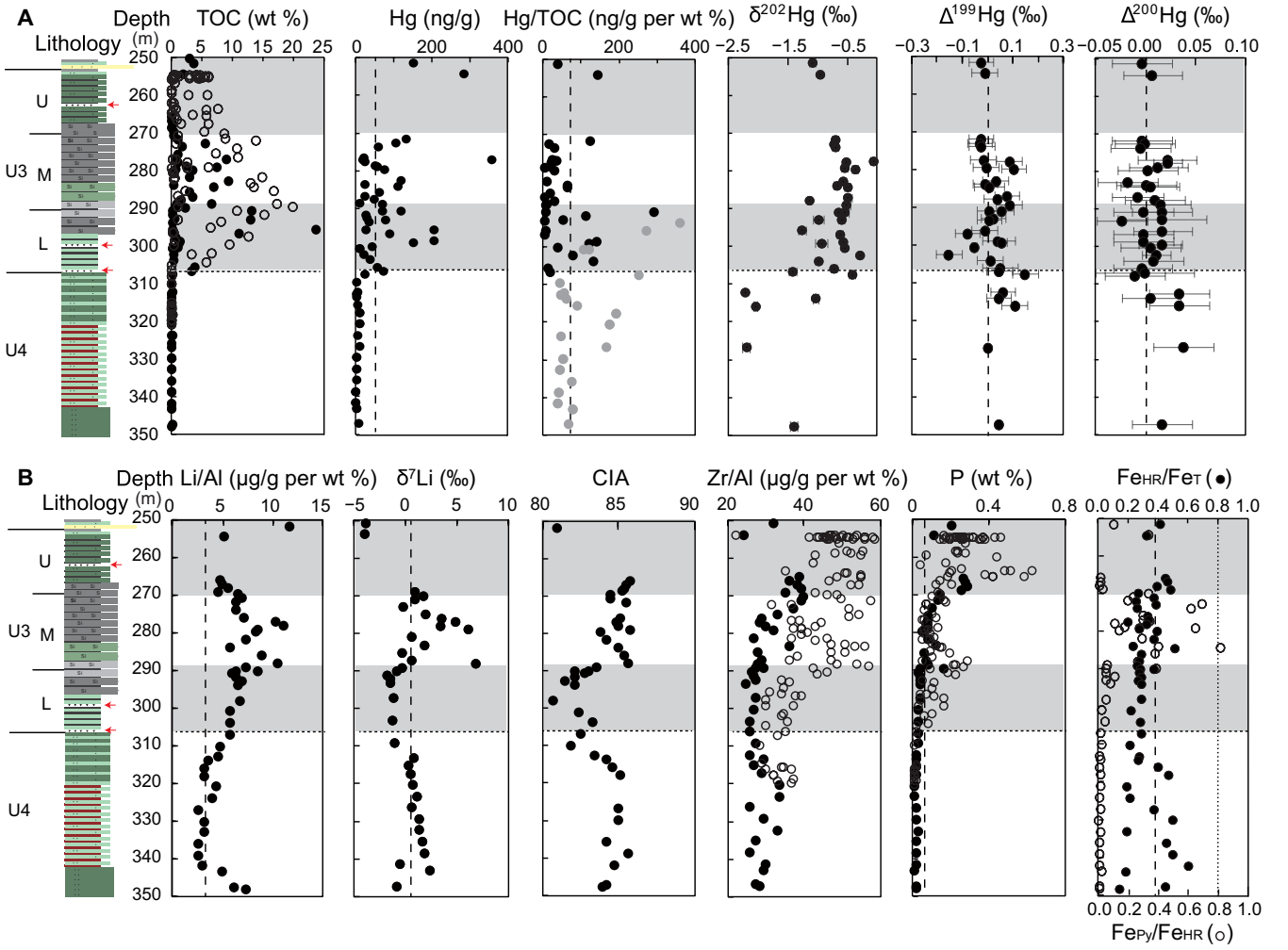

Fig. 3. Geochemical proxies indicative of volcanic activities, continental weathering intensity, nutrient supply, and redox conditions of paleo-water column of U4 and U3 sediments of the Xiamaling Formation. Lithological legends are the same as in Fig. 1. Red arrows represent volcanic ash layers. Black dots and circles in the TOC in (**A**), zircon weight content normalized to aluminium (Zr/Al) and phosphorus (P) panels in (**B**) represent core and outcrop samples, respectively. Gray dots in the mercury normalized to TOC (Hg/TOC) panel in (A) represent the values with TOC value lower than 0.2 wt %. Dash line in the Hg/TOC panel in (A) is the mean value of Phanerozoic sediments (71.9 ng/g per wt %) (*23*). Dash lines in the Hg in (A), lithium weight content normalized to aluminium (Li/Al), lithium isotope composition (δ^7Li), and P panels in (B) are corresponding values of the upper crust, representing 50 ng/g, 2.9 μg/g per wt %, 0.6‰, and 0.07 wt %, respectively (*33*, *65*). Black dots and circles in the ratio of highly reactive Fe to total Fe contents (Fe_{HR}/Fe_T) and ratio of pyrite-Fe to highly reactive Fe (Fe_{Py}/Fe_{HR}) panel in (B) represent their respective ratios. Dash and dot lines in Fe_{HR}/Fe_T and Fe_{Py}/Fe_{HR} panel at 0.38 and 0.80 represent the extreme upper limits for oxic deposition and ferruginous deposition (*37*), respectively. Hg contents, Hg/TOC values, MDF of Hg (δ^{202}Hg), and MIFs of Hg (Δ^{199}Hg, Δ^{200}Hg) in (A) were the proxies of volcanic activities. Li/Al ratios, δ^7Li values, chemical weathering index (CIA), and Zr/Al ratios in (B) were the proxies of continental weathering intensity. P in (B) represent nutrient element. Fe_{HR}/Fe_T and Fe_{Py}/Fe_{HR} in (B) were the proxy of redox conditions of paleo-water column. The CIA values were calculated by using the formula of $CIA = x(Al_2O_3)/\{x(Al_2O_3)/[x(Al_2O_3) + x(CaO^*) + x(Na_2O) + x(K_2O)] \times 100$, where x refers to the mole fraction and CaO* is the CaO in silicates with correction. The TOC, Zr/Al, and Fe species data are cited from (*31*, *32*).

continuous ascending pattern from U4 (31.4 ± 3.6 μg/g per wt %) to U3L (33.4 ± 5.6 μg/g per wt %), further increasing in U3M (41.8 ± 8.8 μg/g per wt %) (Fig. 3B and Table 1). Similarly, P content shows consistent growth from the upper part of U4 (0.02 ± 0.01 wt %) to U3L (0.08 ± 0.06 wt %) and further to U3M (0.12 ± 0.06 wt %) (Fig. 3B and Table 1). Between U4 and U3L, the differences of both CIA values and P contents (including core and outcrop samples) show statistical significance (ANOVA, $P < 0.001$; Fig. 3B and fig. S3). The molar ratios of C:P from the lower, middle, and upper parts of U3 (U3L, U3M, and U3U) sediments are 212:1, 397:1, and 56:1 (Fig. 4), presented as double, nearly quadruple, and half of the Redfield ratio (106:1), respectively, further indicating coupled dynamic variations of continental weathering, nutrient input, as well as MPP at that time.

DISCUSSION

Subaerial volcanic eruptions 1398 Ma ago

In the era preceding industrialization, one of the foremost sources of Hg entering the marine environment was volcanic emissions. This source was particularly crucial, potentially accompanied by contributions from hydrothermal emissions in the deep ocean, which added to the overall Hg content in seawater (*23*). Nonetheless, Hg within

Table 1. The range, mean values, and SDs of the geochemical proxies of U3 and U4 of the Xiamaling Formation. TOC and pyrite data are from (*31*).

Proxy	U4 (347 to 307 m)	U3 (307 to 250 m)	U3L (307 to 290 m)	U3M (290 to 270 m)
TOC (wt %)*	0.04 to 0.2 (0.08 ± 0.04)	0.05 to 23.8 (3.7 ± 4.7)	0.06 to 23.8 (4.5 ± 5.9)	0.1 to 20.0 (4.9 ± 5.4)
Hg (ng/g)	1.6 to 25.4 (6.4 ± 5.3)	10.9 to 356.8 (84.0 ± 76.9)	10.9 to 205.7 (75.8 ± 61.1)	11.6 to 356.8 (76.8 ± 79.0)
Hg/TOC (ng/g per wt %)†	–	6.0 to 294.2 (53.9 ± 61.1)	6.0 to 294.2 (75.0 ± 81.2)	7.4 to 127.3 (33.0 ± 29.0)
δ^{202}Hg (‰)	−2.21 to −0.40‰ (−1.54 ± 0.74‰)	−1.39 to −0.06‰ (−0.67 ± 0.30‰)	−1.39 to −0.26‰ (−0.75 ± 0.32‰)	−1.11 to −0.06‰ (−0.55 ± 0.24‰)
Δ^{199}Hg (‰)	0 to 0.15‰ (0.07 ± 0.05‰)	−0.15 to 0.11‰ (0.01 ± 0.05‰)	−0.15 to 0.06‰ (0.00 ± 0.06‰)	−0.03 to 0.11‰ (0.03 ± 0.05‰)
Δ^{200}Hg (‰)	−0.01 to 0.04‰ (0.02 ± 0.02‰)	−0.02 to 0.02‰ (0.01 ± 0.01‰)	−0.02 to 0.02‰ (0.01 ± 0.01‰)	−0.02 to 0.02‰ (0.01 ± 0.01‰)
Li/Al (μg/g per wt %)	2.6 to 7.4 (3.9 ± 1.4)	4.7 to 11.6 (7.1 ± 1.8)	5.7 to 7.0 (6.3 ± 0.5)	5.7 to 11.1 (8.0 ± 1.6)
δ^{7}Li (‰)	−1.03 to 2.35‰ (0.74 ± 0.99‰)	−3.85 to 6.79‰ (0.74 ± 2.78‰)	−1.76 to −1.16‰ (−1.31 ± 0.31‰)	−0.26 to 6.79‰ (2.25 ± 2.33‰)
CIA	81.9 to 85.7 (84.4 ± 1.0)	80.7 to 85.9 (83.9 ± 1.6)	80.7 to 83.3 (82.2 ± 0.8)	82.2 to 85.9 (84.6 ± 1.1)
Zr/Al (μg/g per wt %)*	26.0 to 37.7 (31.4 ± 3.6)	12.2 to 106.3 (43.5 ± 12.4)	25.2 to 46.6 (33.0 ± 5.6)	27.2 to 58.2 (41.8 ± 8.8)
P (wt %)*	0.02 to 0.04 (0.02 ± 0.01)	0.02 to 0.64 (0.18 ± 0.12)	0.02 to 0.24 (0.08 ± 0.06)	0.06 to 0.29 (0.12 ± 0.06)
Pyrite (wt %)	0.00 to 0.08 (0.03 ± 0.02)	0.01 to 1.64 (0.34 ± 0.37)	0.02 to 0.24 (0.11 ± 0.07)	0.09 to 1.64 (0.44 ± 0.40)

*Data are from outcrop and core, while other proxies only include data from core. †Data do not include the sample values with TOC lower than 0.2 wt %. No available Hg/TOC values for U4 samples for the low TOC values.

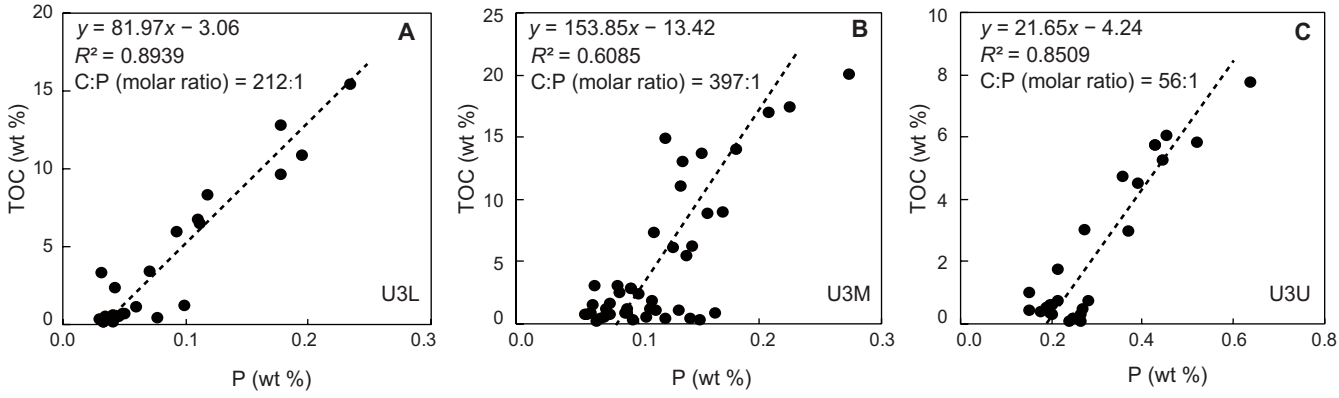

Fig. 4. Relationships of P and TOC of the U3 sediments. (**A**) Lower part of U3 (U3L, 307 to 290 m), with evidence of volcanic eruptions; (**B**) middle part of U3 (U3M, 290 to 270 m), no evidence for volcanic activity; (**C**) upper part of U3 (U3U, 270 to 255 m), with evidence of volcanic eruptions.

seawater predominantly found its way into sediments, forming associations with host phases such as organic matter and sulfide minerals (e.g., pyrite) (*23*). These phases, especially abundant and well-preserved under anoxic or sulfidic conditions, serve as effective sedimentary sinks (*23*). Hence, the enrichment of sedimentary Hg detected in mid-Proterozoic rocks may indicate two distinct possibilities: either a heightened discharge of hydrothermal emissions beneath the ocean's surface or an increased emission of Hg from subaerial volcanic activities. Moreover, these enrichments would likely be influenced by oceanic anoxic events. Our previous studies (*31*, *36*) used geochemical indicators encompassing Fe speciation, the augmentation of redox-sensitive trace metals, and biomarkers linked to anaerobic phototrophs. This evidence allowed us to infer that the paleo-water column of U4 and U3 sediments resembled ancient oxygen minimum zone (OMZ) structures. These zones were characterized by anoxic intermediate water and oxygenated bottom water, the latter of which can be demonstrated by the low ratios (mostly <0.38) of highly reactive Fe to total Fe contents (Fe_{HR}/Fe_T; Fig. 3B) (*37*). However, the increased ratio of pyrite-Fe to highly reactive Fe concentrations (Fe_{py}/Fe_{HR}) from U4 (0.008 ± 0.006) to U3L (0.05 ± 0.03) and the further increase to 0.34 ± 0.23 in U3M (Fig. 3B) are taken to indicate an expansion of marine anoxia in intermediate water.

Our investigation has unveiled compelling correlations between sedimentary Hg and various parameters, reinforcing the role of marine anoxia in Hg enrichment. Notably, a positive linear relationship is evident between Hg and TOC [coefficient of determination (R^2) = 0.59, $P < 0.001$; fig. S6A] and also with pyrite content ($R^2 = 0.37$, $P < 0.001$; fig. S6B) across our samples. The significantly linear positive relationship between sedimentary Hg and P contents ($R^2 = 0.73$, $P < 0.001$; fig. S6C) further highlights the shared sinks for Hg and P. These sinks are attributed to organic matter and/or authigenic

apatite. The latter, involving the formation of mercury phosphate on apatite's active surfaces (*38*), represents a plausible Hg host. Nonetheless, the interplay between sedimentary Hg and clay content demonstrates a distinctive pattern (fig. S6D), deviating from the anticipated relationship based on available mineralogical data (*23*). The reduced Hg content within clay-rich U4 sediments (fig. S6D) is likely a result of insufficient sedimentary organic matter, pyrite, apatite, and, most importantly, a low seawater Hg concentration, influenced by minimal volcanic Hg input (Fig. 5A).

A particularly notable observation lies in the higher Hg content in U3L compared to U4 with significant statistical difference (ANOVA, $P < 0.001$; Fig. 3A and fig. S3H). This disparity indicates an intensified Hg flux from seawater into sediment. However, no statistically significant difference was found in the Hg/TOC values between U3L and U4 (ANOVA, $P = 0.66$; fig. S3I). This might be due to the low TOC values (<0.2 wt %) of U4 sediments (Fig. 3A). The Hg/TOC ratio, an indicative proxy of volcanic activity, may produce misleading outcomes as the TOC values approach the limit of quantitation (~0.05 wt %). The Hg limitation is evident from the U5 sediments, with TOC > 0.2 wt % and a low mean Hg/TOC ratio of 24.6 ng/g per wt % (Fig. 2). This finding further substantiates the notion of diminished seawater Hg concentration and subsequently low Hg flux into sediments. In contrast, some U3L sediments with TOC values higher than 0.2 wt % exhibit slight higher Hg/TOC ratios (75.0 ± 81.2 ng/g per wt %) compared to the mean value of Phanerozoic sediments (71.9 ng/g per wt %) (*23*). These enhanced ratios are concurrent with volcanic ash layers, indicating that the peculiar Hg enrichment in sedimentary records might be attributed to volcanic activity. Similar associations have been identified in U2L (Fig. 2). Akin to these findings, elevated Hg/TOC ratios observed in the ~1.1-Ga Tourist Formation in the Taoudeni Basin, West Africa (*39*), and the ~1.57-Ga Gaoyuzhuang Formation in the Yanliao Basin, North China (*19*), have been attributed to LIP events of that era. This contextualizes the elevated Hg contents and Hg/TOC ratios within U3L and U2 as outcomes of augmented volcanic activity, indicative of an increased inflow of seawater-derived Hg. Although the mean Hg contents are close in the U3L (75.8 ± 61.1 ng/g) and U3M (76.8 ± 79.0 ng/g) sediments, the Hg/TOC values in U3M (33.0 ± 29.0 ng/g) are lower than those in U3L (75.0 ± 81.2 ng/g) with significant statistical difference (ANOVA, $P < 0.001$; Fig. 3A and fig. S3J), consistent with the absence of volcanic

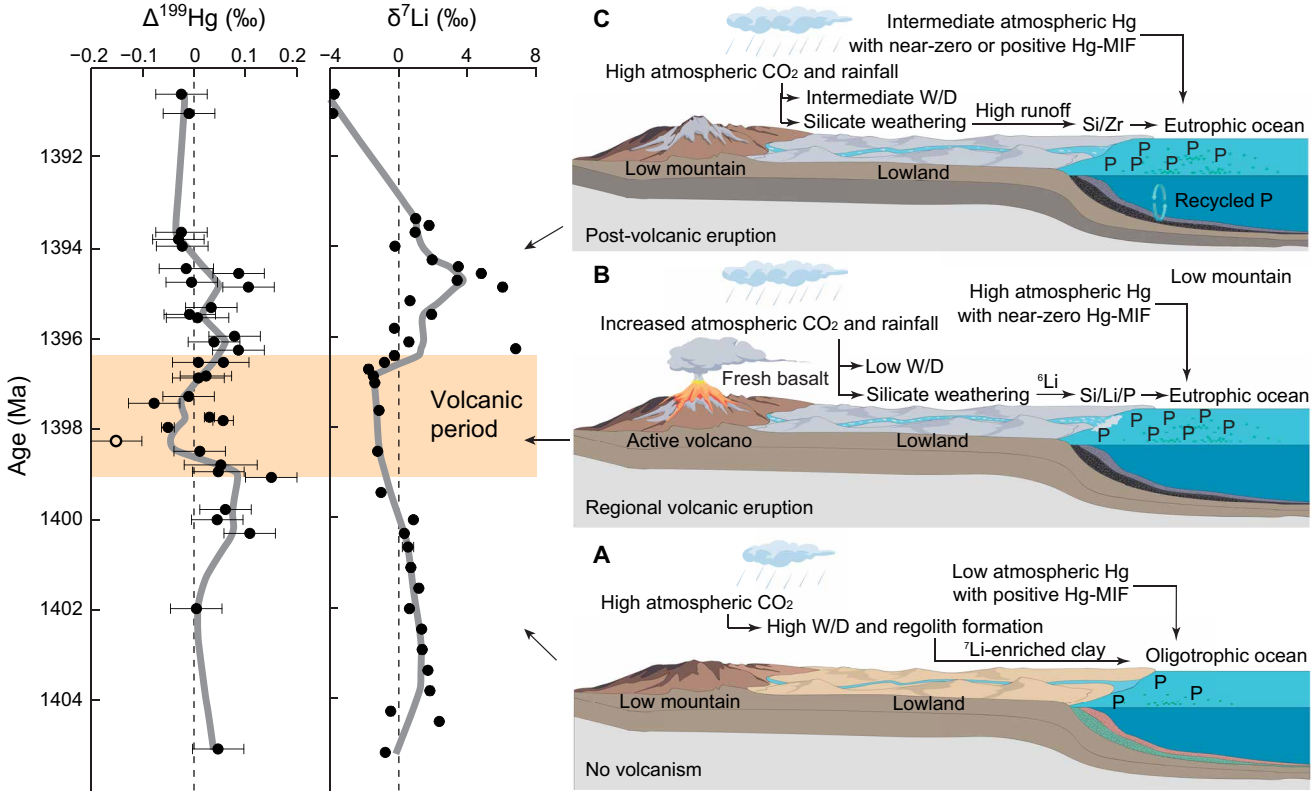

Fig. 5. Schematic diagram of environmental disturbance caused by subaerial volcanic activities during the mid-Proterozoic. The age scale of the MIF of mercury (Hg-MIF; Δ^{199}Hg) and lithium isotope compositions (δ^7Li) of the Xiamaling Formation were obtained from the anchored age (~262.4 m, 1392.2 ± 1.0 Ma) at upper part of U3 (U3U) and an average sedimentary rate of 0.66 cm/ka. The circle Δ^{199}Hg data are abnormal data without unambiguous explanation, see Discussion for details. The gray curves in Δ^{199}Hg and δ^7Li histograms represent Locally Weighted Scatterplot Smoothing (LOWESS) regression trends with 20% smoothing. Error bars for both Δ^{199}Hg and δ^7Li values have been presented. However, because the relatively large data spread, the error bars of Li isotopes are barely visible in the plot. (**A**) U4, without volcanic activities, the sedimentary Hg has positive Hg-MIF values (e.g., Δ^{199}Hg). Continental weathering on the lowland under high atmospheric CO_2 and low rainfall resulted in low terrestrial P flux to ocean. The oligotrophic ocean with P-famine has low MPP and is lack of black shale deposition. (**B**) Lower part of U3 (U3L), coinciding with the subaerial volcanic eruption, the sedimentary Hg increased with near-zero Hg-MIF. Enhanced weathering of the fresh basalt and erosion from the volcano to ocean provide nutrient P and promote the MPP. (**C**) Middle part of U3 (U3M), after the volcanic activities, the sedimentary Hg contents are back to intermediate values with positive Hg-MIF values. Although the terrestrial phosphorus (P) flux to ocean decreased, the recycled P supported high MPP for millions of years or more.

ash layers and an increase in sedimentary organic matter in U3M. The Hg spikes in U3L do not strictly follow those of TOC, indicating that elevated Hg input rather than increased organic matter enrichment is the main factor controlling Hg enrichments.

The isotopic composition of Hg serves as an additional tool to decipher sources and mechanisms underlying Hg enrichment. Mercury emissions from subaerial volcanoes typically exhibit near-zero MIF values with minimal variance (*40*, *41*). In contrast, Hg emanating from remote volcanoes experiences extended atmospheric transport, potentially leading to isotopic fractionation due to atmospheric redox processes (*23*, *42*). These processes, in turn, result in positive Hg-MIF and negative δ^{202}Hg compositions within atmospheric Hg(II) and sediments dominated by atmospheric Hg(II) deposition (*42*). Furthermore, photochemical reduction of aqueous Hg(II) to Hg(0) in the photic zone of euxinic waters, as observed through the end-Permain mass extinction (*43*), could give rise to negative excursions of Hg-MIF of odd-mass isotopes (Δ^{199}Hg and Δ^{201}Hg) within organic-rich sediments. The converse holds true for organic-poor sediments, characterized by predominantly positive Δ^{199}Hg and Δ^{201}Hg values due to a more substantial contribution from atmospheric Hg(II) deposition.

In light of these considerations, the slightly positive Hg-MIF values (Δ^{199}Hg, 0.05 ± 0.04‰; and Δ^{200}Hg, 0.02 ± 0.01‰) and the more negative δ^{202}Hg values (−1.75 ± 0.36‰) evident in U4 sediments, devoid of large amounts of organic content, are comparable to the isotopic signatures found in modern offshore marine sediments (*44*) and mid-Proterozoic marine sediments dominated by background atmospheric Hg deposition (*39*). This alignment suggests a dominant input of Hg from background atmospheric deposition to U4 (Fig. 5A). U3L sediments, hosting volcanic ash layers, exhibit Δ^{199}Hg values closer to zero (0.01 ± 0.05‰, except for a single sample with a Δ^{199}Hg value of −0.15‰) compared to U4. Despite the relatively small variation of Δ^{199}Hg, the difference between U4 and U3L is statistically significant (ANOVA, $P < 0.05$; Fig. 3A and fig. S3B). Concurrent with the shift of Δ^{199}Hg and Δ^{200}Hg also shifted toward near-zero, and δ^{202}Hg shifted to less negative values (around −0.5‰) in U3L (Fig. 3A, fig. S3A, and Table 1). These Hg isotopic signatures in U3L are more consistent with direct volcanic emission (*40*, *41*), thus strongly supporting our hypothesis of subaerial volcanism during the deposition of U3L (Fig. 5B).

One sample from U3L shows a notably negative Δ^{199}Hg value (−0.15‰). Negative Δ^{199}Hg values in sedimentary rocks have been typically ascribed to Hg inputs from terrestrial soils/plants or photic zone euxinia (*45*, *46*). Given the absence of terrestrial biomass during the mid-Proterozoic, terrestrial Hg isotope compositions are posited to align more closely with those of crustal rocks, characterized by near-zero MIF (*47*). Moreover, the robustness of Hg-MIF against diagenesis has been established (*24*), further suggesting that these negative Δ^{199}Hg values may arise from (photo)redox processes involving Hg in seawater before sediment deposition. One conceivable contributor to these negative excursions is marine photic zone euxinia. However, this scenario finds contradiction from iron speciation data (Fig. 3B) and the enrichment of redox-sensitive trace metals, which counter the development of intense euxinic water bodies during U3L sedimentation (*36*). In addition, the prospect of hydrothermal emissions as an explanation for the negative Eu anomaly [$(Eu/Eu^*)_{SN}$; fig. S7] is rendered unlikely. Even in U5 sediments with confirmed hydrothermal activity (*48*), sedimentary Hg contents and Hg/TOC ratios remain minimal (Fig. 2), implying a minor Hg contribution from hydrothermal fluids. Therefore, the transient negative excursion of Δ^{199}Hg in U3L necessitates further exploration.

Compared to U3L, the significantly reduced Hg/TOC ratios in U3M (ANOVA, $P < 0.01$; Fig. 3A and fig. S3J) suggest that local volcanism experienced attenuation post U3L, concurrent with the absence of evident ash layers. However, sporadic instances of heightened Hg/TOC in U3M and U3U indicate that volcanic activities persisted albeit at a reduced frequency, with a confirmed volcanic ash layer discovered at a depth of 262.4 m (Fig. 2B). Consequently, it is plausible to assume that Hg within U3M and U3U sediments arises from a blend of subdued local volcanic emissions and the background atmospheric Hg input (Fig. 5C).

Stratigraphic analyses, involving zircon U-Pb dating (1392 ± 1.0 Ma) of K-bentonite deposits (262.4 m) and the estimated deposition rate of 0.66 cm/thousand year (ka) (*32*), suggest that the two additional volcanic ash layers (307 and 300 m) originated around 1399 to 1398 Ma, with an approximate interval of 1 Ma. In comparison, the temporal distance between the U3L volcanic activity and the 1382-Ma LIP (*30*) extends beyond 16 Ma (fig. S2). This duration exceeds the conventional (<1 to 5 Ma) and maximum (10 to 15 Ma) span associated with a single LIP event (*49*). Notably, volcanic activity during 1.40 to 1.39 Ga has also been reported from other cratons, including the South Laurentian, West Australian, North Australian, Amazonian, and South African (table S1) (*50*–*55*). Despite uncertainties concerning the paleogeographic reconstruction, available evidence indicates that these cratons and the North China Craton were not adjacent to each other during 1.55 to 1.25 Ga (fig. S1A) (*12*). Therefore, this volcanism cannot be simply attributed to the 1382-Ma LIP but more likely represent frequently occurred regional volcanism.

Enhanced continental weathering and terrestrial input after volcanic eruptions

Volcanic activity and the release of acidic gases (CO_2, SO_2, HCl, etc.), coupled with associated temperature increases, have been proposed as triggers or drivers of major environmental disturbances, including intensified continental weathering, alterations in the hydrological cycle, and enhanced riverine transport, as observed during the Permian-Triassic boundary (*56*) and the Palaeocene-Eocene Thermal Maximum (PETM) (*57*, *58*). In our present investigation, we use the detrital silicate fraction as a repository for Li isotopes. Although less studied compared to marine carbonates, this archive is presumed to have originated in riverine catchment areas as a result of weathering, subsequently eroded to its present location (*27*, *28*, *57*). Hence, detrital δ^7Li values are expected to encapsulate local weathering processes occurring in the upstream catchment regions (mainly soils and rivers) that supply material to the depositional site (*57*, *59*). The δ^7Li values in catchment sediments can reflect weathering intensity through two potentially conflicting mechanisms. One mechanism is the inverse relationship between $\Delta^7Li_{fine\text{-}source}$ (difference in δ^7Li between fine-grained sediment and source material) and W/D ratios observed in modern rivers (*27*, *29*). In scenarios of low W/D (high erosion, limited weathering, and a kinetically limited weathering regime), the $\Delta^7Li_{fine\text{-}source}$ hovers around 0‰ due to minimal clay formation, resulting in sediments primarily consisting of source material (*27*). Conversely, in a transport-limited weathering regime characterized by high W/D, the $\Delta^7Li_{fine\text{-}source}$ becomes low (as low as −9‰) due to the generation of isotopically light clays (*27*, *60*).

The magnitudes of detrital δ^7Li excursions are closely linked to paleotopography and surface runoff flux (*61*). Modern comparisons of riverine δ^7Li across diverse geomorphic settings reveal that rivers draining flat lowlands at middle and high latitudes exhibit higher δ^7Li values (associated with intermediate W/D) compared to those originating from mountainous regions (characterized by low W/D) (*61*, *62*). Another explanation for the detrital δ^7Li excursion involves secondary materials primarily formed from surface and, more likely, pore waters within the catchment area, adsorbing Li from various sources. This scenario is especially relevant when considering detrital material of marine sediments, distinct from direct collection of river deposits. Consequently, detrital δ^7Li can manifest both negative excursions (e.g., PETM's hothouse phase with declining W/D) (*57*) and positive excursions (e.g., Hirnantian glaciation's icehouse phase with increased W/D) (*59*). Similar patterns have been observed in modern rivers at different latitudes (*28*), where intermediate W/D corresponds to elevated detrital δ^7Li values (often surpassing initial rock values) (*59*). In this context, detrital δ^7Li would generally follow a boomerang plot with W/D (*28*, *29*, *57*).

In this study, we use detrital Li contents and isotopic compositions (δ^7Li) as proxies for continental weathering and terrestrial input. The U4 sediments are characterized by low Li/Al ratios (3.9 ± 1.4 μg/g per wt %), intermediate δ^7Li values (0.74 ± 0.99‰), high CIA values (84.4 ± 1.0), and low Zr/Al ratios (31.4 ± 3.6 μg/g per wt %) (Fig. 3B and Table 1). Notably, during the mid-Proterozoic, a greenhouse-dominated climate prevailed, marked by elevated atmospheric pCO_2 level (~2 to 50 times modern level) (*63*). Paleomagnetic reconstruction places the Yanliao Basin, housing the Xiamaling Formation sediments, within the northern tropics (10°N to 20°N) during 1400 to 1300 Ma (fig. S1A), positioning it within the high rainfall regions of the Hadley Cell. The Yanliao Basin was encompassed by several paleolowlands (e.g., Shanhaiguan and Shanxi), and it was generally a period of relative orogenic quiescence and a lowland landscape (Fig. 5A) (*6*). Collectively, these climatic and paleogeographic conditions likely fostered heightened chemical weathering while maintaining relatively low denudation rates (Fig. 5A), sustaining a high-intensity supply-limited weathering regime (*64*).

The negative δ^7Li excursion (−2.0‰) observed from U4 to U3L is comparable yet smaller than the detrital δ^7Li excursion induced by volcanic activity during the PETM, which recorded around −3‰ (*57*). Given the extended duration of our detrital δ^7Li excursion (spanning several million years), it is probable that the δ^7Li excursion signifies changes in the steady-state composition of seawater (generally of smaller magnitude), as opposed to dynamic non–steady-state variations seen during the PETM (lasting only tens of thousands of years) (*57*). Meanwhile, the emergence of fresh rock facilitated denudation rates to ensure high capacity for debris transport with reduced chemical weathering, i.e., low W/D ratios (*28*). From U4 to U3L, the former can be reflected by the statistically significant increase of Li/Al ratios (ANOVA, $P < 0.001$; Fig. 3B and fig. S3D), and the latter is from the significant decrease of CIA values (ANOVA, $P < 0.001$; Fig. 3B and fig. S3F). Both factors would lead δ^7Li values to approach those of the continental crust (~0.6‰) (*65*). Reciprocal variations of Li/Al and δ^7Li in U3L point to an intensified continental denudation process that removed more Li-enriched detrital material from land to ocean (Fig. 5B). A reverse relationship of Li/Al ratios and W/D values has also been found in modern river sediments (*27*). Analogous behavior has been documented during periods characterized by volcanic eruptions and CO_2 release in the Phanerozoic, such as the Cretaceous Oceanic Anoxic Events (*66*, *67*) and the PETM (*57*, *68*). Consequently, it is conjectured that the enhanced erosion and reduced W/D values during U3L deposition resulted from an accelerated hydrological cycle, akin to conditions observed in certain Phanerozoic and modern sedimentary records (*28*, *57*, *66*, *67*).

Compared to U3L sediments, U3M sediments exhibit elevated values of Li/Al (ANOVA, $P < 0.01$; fig. S3K) and δ^7Li values ($P < 0.001$; fig. S3L), featured by notable statistical significances (Fig. 3B and Table 1). As discussed previously, the evidence from Hg content and isotopic data indicates diminished volcanism and decreased detrital Li input from land to ocean. Simultaneously, the transition from U3L to U3M witnessed an increase in quartz content and a decrease in clay content (fig. S7). For U3M samples with quartz content exceeding 70% (designated as chert), strong positive linear correlations between quartz content and Li/Al ratios ($R^2 = 0.87$; fig. S8A) as well as δ^7Li values ($R^2 = 0.95$; fig. S8B) are evident, indicating the critical role of authigenic quartz in sequestering Li from seawater. Even so, Li contents in U3M are generally low (mean value, 36.3 ± 8.2 μg/g), which are consistent with a detrital origin with Li content lower than 50 μg/g and against with the authigenic clay with Li content up to 500 μg/g (*69*).

The cyclic alternation of cherts or green mudstones with black shales in U3 has been attributed to Milankovitch-scale orbital climate forcing, during which the Yanliao Basin occupied the downwelling limb of the Hadley Cell, with alternating intensities of high and low trade winds (*32*). The shifting positions of the Hadley Cell could influence the hydrological cycle and terrestrial weathering intensity (*70*). However, existing evidence indicates no notable changes in climate zones between the depositions of U4 and U3. It has been suggested that the Yanliao Basin was situated in the descending limb of the Hadley Cell for both units (*31*). Thus, variations in Li isotopes are most likely attributed to changes in volcanism-related weathering intensity. The post-volcanic weathering conditions were probably kinetically limited, yielding high dissolved δ^7Li and low detrital sediment δ^7Li values (Fig. 5C) (*28*, *57*).

While it is difficult to directly quantify the palaeo-weathering regime if weathering and denudation rates are not directly known, it is possible to use modern river sediment relationships to make estimates of the changes. Notably, the detrital sediment values from this study, especially from U4 and U3M, have higher δ^7Li than the initial rock (Fig. 3B). Thus, a Rayleigh-like fractionation behavior, which allows sediment δ^7Li that is higher than the rock, must be occurring, as also observed in modern Icelandic river sediments (*29*). Given potential differences between modern and Proterozoic basaltic weathering, the weathering regime started at a W/D > 0.1 (the high side of intermediate weathering intensity, also observed globally during the Middle-Eocene) (*68*) during U4 deposition. It then decreased to W/D of ~0.002 (low weathering intensity) during U3L deposition and then subsequently increased to a W/D of ~0.008 to 0.04 (on the low side of intermediate weathering intensity) during U3M deposition.

Enhanced nutrient fluxes and MPP following the subaerial volcanism

Continental weathering and riverine transport stand as the principal sources of bio-essential nutrients (e.g., P) to the oceans. However, during the mid-Proterozoic era, the absence of large-scale orogenic activity could have considerably curtailed the flux of continental weathering-derived P (*8*). Potential inorganic P sinks in

the predominately anoxic mid-Proterozoic oceans include authigenic calcium fluorapatite (*71*), vivianite (*72*), and green rust (*73*). A P-depleted seawater condition has been inferred for the mid-Proterozoic, as demonstrated in the U4 sediment record (Fig. 5A), which exhibits a lower P content (0.02 ± 0.01 wt %; Fig. 3B and Table 1) compared to the upper continental crust (0.06 wt %) (*33*) and pre-Cryogenian samples (0.05 ± 0.003 wt %) (*72*). Subsequent to the volcanic events at the base of U3, the mean sedimentary P content of U3 rises to 0.18 ± 0.12 wt %, about nine times higher than that of U4 sediments (Fig. 3B and Table 1), and is comparable to the mean value for post-Tonian samples (less than 720 Ma) (0.21 ± 0.02 wt %) (*72*). This substantial increase from U4 to U3 cannot be attributed solely to potential variations in water chemistry, as both U4 and U3 sedimentation occurred under similar conditions within the OMZ settings (*31*).

Alternatively, the enrichment of P in U3 sediments could signify an intensified continental influx of P prompted by volcanic activity (Fig. 5B). Volcanic P sources have been proposed as a mechanism for ocean fertilization throughout Earth history (*8*). Similar to observations during the PETM, escalated weathering and erosion facilitated the transport of dissolved P and other nutrients to the ocean, potentially boosting MPP and aligning local organic carbon burial (*57*, *68*). Coinciding with this scenario, the TOC content of U3 sediments increased to ~24 wt % after volcanic activity (Fig. 3A), indicative of heightened MPP and/or enhanced preservation efficiency. The C:P molar ratio (212:1; Fig. 4A) of U3L sediments is double of the Redfield ratio (106:1), suggesting that, when organic matter settled in coeval oceanic water column, more P than C was released into the ocean through partial degradation (*9*). A similar phenomenon is observed in U3M sediments with a C:P molar ratio of 397:1 (Fig. 4B). This implies that recycled P further bolstered MPP and the deposition of organic carbon (Fig. 5C) and could sustain MPP for millions of years or even longer. The impact of P recycling during U3 deposition can be evaluated by drawing parallels with the modern Peruvian margin sediments, which is also deposited under OMZ structures. The benthic flux of phosphate can reach levels as high as 292 mmol m^{-2} $year^{-1}$ through the Peruvian shelf and OMZ core, coinciding with high organic carbon degradation rates (*74*).

The identified volcanic activities coincide with the onset of a well-documented mid-Proterozoic oxygenation event (*36*). As modeled by Laakso and Schrag (*11*), organic carbon burial rate is very sensitive to P supply in the Proterozoic oceans. It is likely that a volcanism-induced nutrient surplus and a correspondingly elevated MPP could have resulted in a shift to a more oxygenated environment, because net burial of organic carbon results in a rise in atmospheric oxygen. Such a scenario is in line with the high TOC concentrations (a maximum value of 23.8 wt %) and a positive $\delta^{13}C_{org}$ excursion (an excursion of 6‰) throughout the deposition of U3 (*36*). Because both TOC and $\delta^{13}C_{org}$ are typically considered as local proxies, whether an intrinsic relationship between the observed geochemical shifts and the oxygenation event can be established would require data from additional profiles worldwide. However, sediments from the time-equivalent Velkerri Formation in North Australia are also enriched in organic matter (fig. S2) and has been suggested to record the influence of mafic rocks (*55*, *75*). Thus, an organic burial event occurred at least in two cratons, which might have consumed CO_2 and released substantial oxygen into the atmosphere.

It is difficult to constrain the scale of mid-Proterozoic volcanisms that are needed to drive a global oxygenation event. Ash layer is conclusive evidence of explosive eruptions, but it may reflect changes in eruption style and may not be indicative of overall volcanic activity due to the biogeochemical and halmyrolysis processes (*76*). The best demonstration of the answer is to compare to more recent examples. For the late Pleistocene and Holocene volcanism in the tropical region of Sumatra, most tephra layers from small subaerial volcanic eruptions (e.g., volcanic explosive index < 5) become invisible in offshore sediments due to biogeochemical and halmyrolysis processes, especially at a low sedimentation rate (1.6 ± 1.0 cm/ka) (*76*). Given that, the visible ash layers with a thickness of 1 to 10 cm (Fig. 1, B to D) preserved in the Xiamaling Formation might originate from volcanoes with a volcanic explosive index of >5 to 7. Such volcano should have a volume of ejecta over 1 to 100 km^3 or larger (*77*). The drivers of enhanced subaerial volcanic activity are still under debate. Because of their occurrence being mostly related to large-scale continental rifting and breakup of Columbia (Nuna) supercontinent (*53*, *55*), it could be related to interior superplume activities and/or encircling subduction systems (*78*). Nevertheless, our results emphasize that subaerial volcanism and its corresponding effect on weathering can break the long-term stasis of the mid-Proterozoic.

MATERIALS AND METHODS

Samples

Samples analyzed here were collected as a core, which was drilled with fresh water to minimize contamination from drill fluids. For the poor recovery of the U3 rocks in the core, only a few organic-rich samples were available to do isotopic composition analyses of Hg and Li. To better demonstrate the situation of black shales in U3, the published TOC, P, and Zr/Al data from fresh outcrop samples (*32*), which collected and analyzed in 10 years ago, are also used for statistical analysis.

Mineralogical and elemental analysis

Mineralogy of samples was determined through x-ray diffraction analysis with a Rigaku MiniFlex X-ray diffractometer using a 600-W Cu-kα source. The measurement was performed at the Key Laboratory of Petroleum Geochemistry, China National Petroleum Corporation, and following procedures described in (*48*). Major and trace elements were determined at the Analytical Laboratory of Beijing Research Institute of Uranium Geology, China National Nuclear Corporation, after the methods described in (*32*).

Mercury contents and isotopic composition analyses

Mercury (Hg) contents were analyzed on a Lumex R-915F Hg Analyzer at Tianjin University. Mercury in samples was released as Hg(0) vapor by pyrolysis at a temperature of ~750°C and then measured by a cold vapor atomic absorption spectroscopy with a detection limit lower than 0.5 ng/g. Two certified reference materials, GBW07311 (GSD-11, freshwater sediment, with an average Hg concentration of 72 ng/g) and GBW07405 (GSS-5, yellow-red soil, with an average Hg concentration of 320 ng/g), were measured repeatedly alongside samples to monitor analytical accuracy and reproducibility. Our measurements of GBW07311 and GBW07405 yielded average Hg concentrations of 72.2 ± 2.8 ng/g (1SD, $n = 3$) and 319.9 ± 13.1 ng/g (1SD, $n = 23$), respectively, which are consistent with their certified values.

Mercury isotopes were analyzed using a multi-collector inductively coupled plasma mass spectrometer (MC-ICPMS; Neptune Plus, Thermo Fisher Scientific) at Tianjin University based on previously described methods (*39*). Before isotope analysis, Hg in samples was first extracted by acid digestion and then purified by ion-exchange chromatography. Briefly, powdered samples were weighed into 30-ml Teflon beakers and digested with a mixture of trace metal grade concentrated acids containing HNO_3, HCl, and BrCl (2 M) with a volume ratio of 12:6:1 at ~100°C for 48 hours. After centrifugation, an anion-exchange chromatographic method was applied to separate Hg from matrix. The overall Hg yield of the digestion and anion-exchange chromatographic procedures was 102 ± 7% (2SD, n = 113) for all samples. Procedural blanks were processed alongside samples, as were three standard reference materials, including NIST 2702 (marine sediment), GBW07311 (freshwater sediment), and GBW07407 (laterite), and the pure Hg isotope standard NIST SRM 3133. Recoveries for NIST SRM 3133 and the reference materials were 100 ± 5% (2SD, n = 8). Mercury concentrations in procedural blanks were typically less than 1% of the Hg present in samples.

Mercury isotope ratios in the purified solution were analyzed at ~1 to 1.5 ng/g. The Hg in the diluted solutions is first reduced by $SnCl_2$ (3%, w/v) to gaseous Hg(0), which is then carried into the plasma of MC-ICPMS by Hg-free argon gas. Simultaneously, thallium (Tl) aerosol (NIST SRM 997) generated by Aridus II desolvator was introduced together with Hg(0) vapor into the plasma. Five Hg isotopes (^{198}Hg, ^{199}Hg, ^{200}Hg, ^{201}Hg, and ^{202}Hg) and two Tl isotopes (^{203}Tl and ^{205}Tl) were simultaneously measured via Faraday cups. Instrumental mass bias was corrected for using a combination of internal calibration with measured ^{205}Tl/^{203}Tl ratios and standard-sample-standard bracketing (relative to the NIST SRM 3133 Hg standard). The bracketing standard was matched to samples in terms of both matrix and Hg concentration (less than 10% difference). On-peak zero corrections were applied to all measured masses. Mercury isotope compositions are reported using δ notation defined by the following equation:

$$\delta^{x}\mathrm{Hg} = [(^{x}\mathrm{Hg}/^{198}\mathrm{Hg})_{\mathrm{sample}} / (^{x}\mathrm{Hg}/^{198}\mathrm{Hg})_{\mathrm{std}} - 1] \times 1000$$

where ^{x}Hg is ^{199}Hg, ^{200}Hg, ^{201}Hg, or ^{202}Hg, and "std" represents the NIST SRM 3133 mercury standard. The MDF is reported as δ^{202}Hg, and MIF is reported as the capital delta notation (Δ) according to the following equation:

$$\Delta^{x}\mathrm{Hg} = \delta^{x}\mathrm{Hg} - (\delta^{202}\mathrm{Hg} \times \beta)$$

where x is the mass number of Hg isotope 199, 200, and 201. β is a scaling constant used to estimate the theoretical kinetic MDF, and it is 0.2520, 0.5024, and 0.7520 for ^{199}Hg, ^{200}Hg, and ^{201}Hg, respectively.

Each sample was measured twice, and a commonly used reference standard NIST SRM 8610 (UM Almadén) was measured every five samples to monitor instrument performance. The average of all NIST 8610 is δ^{202}Hg = −0.53 ± 0.05‰, Δ^{199}Hg = −0.03 ± 0.05‰, and Δ^{200}Hg = 0.00 ± 0.03‰ (2SD, n = 12). The certified reference material GBW07311 yielded average δ^{202}Hg, Δ^{199}Hg, and Δ^{200}Hg values of −0.55 ± 0.02‰, −0.26 ± 0.01‰, and − 0.01 ± 0.01‰ (n = 2, 2SE), respectively. The measured values of NIST 8610 and GBW07311 are both consistent with published values. All isotope data are reported as either 2SE of sample replicates or 2SD of all measurements of the NIST 8610, whichever is higher.

Lithium isotopic composition analysis

Chemical procedures and determination of Li isotopes were performed at the State Key Laboratory of ore deposit geochemistry, Institute of Geochemistry, Chinese Academy of Sciences. A two-step column chemistry was used to isolate Li from the sample matrix, following the method described in (*79*). Briefly, sample solutions first passed through a column loaded with 7 ml of Dowex 50WX8 (200 to 400 mesh) resin for the removal of most matrix elements. Residual Na in samples was further eliminated through another column loaded with 2.5 ml of the resin. Li isotope ratios of the purified solutions were obtained using the standard-sample bracketing protocol in a Neptune MC-ICPMS. All data were reported per mil relative to IRMM-016. To monitor the isotopic fractionation during the chemical pretreatment, seawater (CASS-5; National Research Council of Canada), rock references (BCR-2), and Li isotopes standard solutions (IRMM-016) were treated as unknown samples. The results yielded δ^{7}Li values of 30.91 ± 0.16‰ for CASS-5, 2.69 ± 0.31‰ for BCR-2, and −0.01 ± 0.17‰ for IRMM-016.

Supplementary Materials

This PDF file includes:

Figs. S1 to S8
Table S1
Legend for data S1

Other Supplementary Material for this manuscript includes the following:

Data S1

REFERENCES AND NOTES

1. R. E. Ernst, A. J. Dickson, A. Bekker, *Large Igneous Provinces: A Driver of Global Environmental and Biotic Changes* (Wiley, 2021).
2. A. H. Knoll, M. A. Nowak, The timetable of evolution. *Sci. Adv.* **3**, e1603076 (2017).
3. L. Miao, Z. Yin, A. H. Knoll, Y. Qu, M. Zhu, 1.63-billion-year-old multicellular eukaryotes from the Chuanlinggou Formation in North China. *Sci. Adv.* **10**, eadk3208 (2024).
4. A. Prokoph, G. A. Shields, J. Veizer, Compilation and time-series analysis of a marine carbonate δ^{18}O, δ^{13}C, ^{87}Sr/^{86}Sr and δ^{34}S database through Earth history. *Earth Sci. Rev.* **87**, 113–133 (2008).
5. T. W. Lyons, C. T. Reinhard, N. J. Planavsky, The rise of oxygen in Earth's early ocean and atmosphere. *Nature* **506**, 307–315 (2014).
6. M. Tang, X. Chu, J. Hao, B. Shen, Orogenic quiescence in Earth's middle age. *Science* **371**, 728–731 (2021).
7. N. M. W. Roberts, The boring billion?–Lid tectonics, continental growth and environmental change associated with the Columbia supercontinent. *Geosci. Front.* **4**, 681–691 (2013).
8. F. Horton, Did phosphorus derived from the weathering of large igneous provinces fertilize the neoproterozoic ocean? *Geochem. Geophys. Geosyst.* **16**, 1723–1738 (2015).
9. D. E. Canfield, C. J. Bjerrum, S. Zhang, H. Wang, X. Wang, The modern phosphorus cycle informs interpretations of Mesoproterozoic Era phosphorus dynamics. *Earth Sci. Rev.* **208**, 103267 (2020).
10. A. D. Anbar, A. H. Knoll, Proterozoic ocean chemistry and evolution: A bioinorganic bridge? *Science* **297**, 1137–1142 (2002).
11. T. A. Laakso, D. P. Schrag, A small marine biosphere in the Proterozoic. *Geobiology* **17**, 161–171 (2019).
12. S.-H. Zhang, R. E. Ernst, J.-L. Pei, Y. Zhao, G.-H. Hu, "Large igneous provinces (LIPs) and anoxia events in 'The Boring Billion'" in *Large Igneous Provinces: A Driver of Global Environmental and Biotic Changes*, R. Ernst, A. J. Dickson, A. Bekker, Eds. (Wiley, 2021), pp. 449–486.
13. D. E. Canfield, S. Zhang, A. B. Frank, X. Wang, H. Wang, J. Su, Y. Ye, R. Frei, Highly fractionated chromium isotopes in Mesoproterozoic-aged shales and atmospheric oxygen. *Nat. Commun.* **9**, 2871 (2018).
14. Y. Ye, S. Zhang, H. Wang, X. Wang, C. Tan, M. Li, C. Wu, D. E. Canfield, Black shale Mo isotope record reveals dynamic ocean redox during the Mesoproterozoic Era. *Geochem. Perspect. Lett.* **18**, 16–21 (2021).

15. G. J. Gilleaudeau, S. J. Romaniello, G. Luo, A. J. Kaufman, F. Zhang, R. M. Klaebe, L. C. Kah, K. Azmy, J. K. Bartley, W. Zheng, A. H. Knoll, A. D. Anbar, Uranium isotope evidence for limited euxinia in mid-Proterozoic oceans. *Earth Planet. Sci. Lett.* **521**, 150–157 (2019).
16. N. Tribovillard, T. J. Algeo, T. Lyons, A. Riboulleau, Trace metals as paleoredox and paleoproductivity proxies: An update. *Chem. Geol.* **232**, 12–32 (2006).
17. W. W. Bennett, D. E. Canfield, Redox-sensitive trace metals as paleoredox proxies: A review and analysis of data from modern sediments. *Earth Sci. Rev.* **204**, 103175 (2020).
18. C. W. Diamond, R. E. Ernst, S.-H. Zhang, T. W. Lyons, "Breaking the Boring Billion: A case for solid-Earth processes as drivers of system-scale environmental variability during the mid-Proterozoic" in *Large Igneous Provinces: A Driver of Global Environmental and Biotic Changes*, R. Ernst, A. J. Dickson, A. Bekker, Eds. (Wiley, 2021), pp. 487–501.
19. D. Tang, X. Fu, X. Shi, L. Zhou, W. Zheng, C. Li, D. Xu, X. Zhou, B. Xie, X. Zhu, G. Jiang, Enhanced weathering triggered the transient oxygenation event at ~1.57 Ga. *Geophys. Res. Lett.* **49**, e2022GL099018 (2022).
20. D. E. Canfield, The evolution of the Earth surface sulfur reservoir. *Am. J. Sci.* **304**, 839–861 (2004).
21. V. A. Prokin, F. P. Buslaev, Massive copper-zinc sulphide deposits in the Urals. *Ore Geol. Rev.* **14**, 1–69 (1998).
22. J. Meixnerová, J. D. Blum, M. W. Johnson, E. E. Stüeken, M. A. Kipp, A. D. Anbar, R. Buick, Mercury abundance and isotopic composition indicate subaerial volcanism prior to the end-Archean "whiff" of oxygen. *Proc. Natl. Acad. Sci. U.S.A.* **118**, e2107511118 (2021).
23. S. E. Grasby, T. R. Them, Z. Chen, R. Yin, O. H. Ardakani, Mercury as a proxy for volcanic emissions in the geologic record. *Earth Sci. Rev.* **196**, 102880 (2019).
24. Z. Liu, H. Tian, R. Yin, D. Chen, H. Gai, Mercury loss and isotope fractionation during thermal maturation of organic-rich mudrocks. *Chem. Geol.* **612**, 121144 (2022).
25. S. Misra, P. N. Froelich, Lithium isotope history of cenozoic seawater: Changes in silicate weathering and reverse weathering. *Science* **335**, 818–823 (2012).
26. P. A. E. Pogge von Strandmann, S. A. Kasemann, J. B. Wimpenny, Lithium and lithium isotopes in Earth's surface cycles. *Elements* **16**, 253–258 (2020).
27. M. Dellinger, J. Bouchez, J. Gaillardet, L. Faure, J. Moureau, Tracing weathering regimes using the lithium isotope composition of detrital sediments. *Geology* **45**, 411–414 (2017).
28. M. Dellinger, J. Gaillardet, J. Bouchez, D. Calmels, P. Louvat, A. Dosseto, C. Gorge, L. Alanoca, L. Maurice, Riverine Li isotope fractionation in the Amazon River basin controlled by the weathering regimes. *Geochim. Cosmochim. Acta* **164**, 71–93 (2015).
29. P. A. E. Pogge von Strandmann, L. R. Cosford, C. Y. Liu, X. Liu, A. J. Krause, D. J. Wilson, X. He, A. J. McCoy-West, S. R. Gislason, K. W. Burton, Assessing hydrological controls on the lithium isotope weathering tracer. *Chem. Geol.* **642**, 121801 (2023).
30. S.-H. Zhang, R. E. Ernst, J.-L. Pei, Y. Zhao, M.-F. Zhou, G.-H. Hu, A temporal and causal link between ca. 1380 Ma large igneous provinces and black shales: Implications for the Mesoproterozoic time scale and paleoenvironment: Implications for the Mesoproterozoic time scale and paleoenvironment. *Geology* **46**, 963–966 (2018).
31. X. Wang, S. Zhang, H. Wang, C. J. Bjerrum, E. U. Hammarlund, E. R. Haxen, J. Su, Y. Wang, D. E. Canfield, Oxygen, climate and the chemical evolution of a 1400 million year old tropical marine setting. *Am. J. Sci.* **317**, 861–900 (2017).
32. S. Zhang, X. Wang, E. U. Hammarlund, H. Wang, M. M. Costa, C. J. Bjerrum, J. N. Connelly, B. Zhang, L. Bian, D. E. Canfield, Orbital forcing of climate 1.4 billion years ago. *Proc. Natl. Acad. Sci. U.S.A.* **112**, E1406–E1413 (2015).
33. R. L. Rudnick, S. Gao, *Composition of the Continental Crust* in *Treatise on Geochemistry*, H. D. Holland, K. K. Turekian, Eds. (Elsevier, ed. 2, 2014), pp. 1–51.
34. C. M. Fedo, H. W. Nesbitt, G. M. Young, Unraveling the effects of potassium metasomatism in sedimentary rocks and paleosols, with implications for paleoweathering conditions and provenance. *Geology* **23**, 921–924 (1995).
35. N. Jiang, J. Guo, M. Zhai, Nature and origin of the Wenquan granite: Implications for the provenance of Proterozoic A-type granites in the North China craton. *J. Asian Earth Sci.* **42**, 76–82 (2011).
36. S. Zhang, X. Wang, H. Wang, C. J. Bjerrum, E. U. Hammarlund, M. M. Costa, J. N. Connelly, B. Zhang, J. Su, D. E. Canfield, Sufficient oxygen for animal respiration 1,400 million years ago. *Proc. Natl. Acad. Sci. U.S.A.* **113**, 1731–1736 (2016).
37. S. W. Poulton, D. E. Canfield, Ferruginous conditions: A dominant feature of the ocean through earth's history. *Elements* **7**, 107–112 (2011).
38. J. Oliva, J. De Pablo, J. Cortina, J. Cama, C. Ayora, Removal of cadmium, copper, nickel, cobalt and mercury from water by Apatite II™: Column experiments. *J. Hazard. Mater.* **194**, 312–323 (2011).
39. W. Zheng, G. J. Gilleaudeau, L. C. Kah, A. D. Anbar, Mercury isotope signatures record photic zone euxinia in the Mesoproterozoic ocean. *Proc. Natl. Acad. Sci. U.S.A.* **115**, 10594–10599 (2018).
40. M. Si, D. S. McLagan, A. Mazot, N. Szponar, B. Bergquist, Y. D. Lei, C. P. J. Mitchell, F. Wania, Measurement of atmospheric mercury over volcanic and fumarolic regions on the North Island of New Zealand using passive air samplers. *ACS Earth Space Chem.* **4**, 2435–2443 (2020).
41. T. Zambardi, J. E. Sonke, J. P. Toutain, F. Sortino, H. Shinohara, Mercury emissions and stable isotopic compositions at Vulcano Island (Italy). *Earth Planet. Sci. Lett.* **277**, 236–243 (2009).
42. A. M. Thibodeau, B. A. Bergquist, Do mercury isotopes record the signature of massive volcanism in marine sedimentary records? *Geology* **45**, 95–96 (2017).
43. R. Sun, Y. Liu, J. E. Sonke, Z. Feifei, Y. Zhao, Y. Zhang, J. Chen, C. Q. Liu, S. Shen, A. D. Anbar, W. Zheng, Mercury isotope evidence for marine photic zone euxinia across the end-Permian mass extinction. *Commun. Earth Environ.* **4**, 159 (2023).
44. N. Ogrinc, H. Hintelmann, J. Kotnik, M. Horvat, N. Pirrone, Sources of mercury in deep-sea sediments of the Mediterranean Sea as revealed by mercury stable isotopes. *Sci. Rep.* **9**, 11626 (2019).
45. W. Zheng, A. Zhou, S. K. Sahoo, M. R. Nolan, C. M. Ostrander, R. Sun, A. D. Anbar, S. Xiao, J. Chen, Recurrent photic zone euxinia limited ocean oxygenation and animal evolution during the Ediacaran. *Nat. Commun.* **14**, 3920 (2023).
46. W. Zheng, G. J. Gilleaudeau, T. J. Algeo, Y. Zhao, Y. Song, Y. Zhang, S. K. Sahoo, A. D. Anbar, S. K. Carmichael, S. Xie, C.-Q. Liu, J. Chen, Mercury isotope evidence for recurrent photic-zone euxinia triggered by enhanced terrestrial nutrient inputs during the Late Devonian mass extinction. *Earth Planet. Sci. Lett.* **613**, 118175 (2023).
47. J. D. Blum, L. S. Sherman, M. W. Johnson, Mercury isotopes in Earth and environmental sciences. *Annu. Rev. Earth Planet. Sci.* **42**, 249–269 (2014).
48. H. J. Wang, Y. T. Ye, Y. Deng, X. M. Wang, E. U. Hammarlund, H. F. Fan, D. E. Canfield, S. C. Zhang, Isotope evidence for the coupled iron and carbon cycles 1.4 billion years ago. *Geochem. Perspect. Lett.* **21**, 1–6 (2022).
49. S. E. Bryan, R. E. Ernst, Revised definition of Large Igneous Provinces (LIPs). *Earth Sci. Rev.* **86**, 175–202 (2008).
50. M. E. Bickford, W. R. Van Schmus, K. E. Karlstrom, P. A. Mueller, G. D. Kamenov, Mesoproterozoic-trans-Laurentian magmatism: A synthesis of continent-wide age distributions, new SIMS U-Pb ages, zircon saturation temperatures, and Hf and Nd isotopic compositions. *Precambrian Res.* **265**, 286–312 (2015).
51. J. C. Stark, X. C. Wang, Z. X. Li, S. W. Denyszyn, B. Rasmussen, J. W. Zi, 1.39 Ga mafic dyke swarm in southwestern Yilgarn Craton marks Nuna to Rodinia transition in the West Australian Craton. *Precambrian Res.* **316**, 291–304 (2018).
52. M. A. Elburg, R. G. Cawthorn, Source and evolution of the alkaline Pilanesberg Complex, South Africa. *Chem. Geol.* **455**, 148–165 (2017).
53. A. Bonilla, J. A. Franco Victoria, T. Cramer, J. De Grave, S. Nachtergaele, N. Cogné, A. Piraquive, The NW Amazonian Craton in Guainía and Vaupés departments, Colombia: Evidence of a Mesoproterozoic thermal event from apatite LA-ICP-MS U-Pb geochronology and its relation to continental rifting. *Precambrian Res.* **395**, 107148 (2023).
54. B. Kendall, R. A. Creaser, G. W. Gordon, A. D. Anbar, Re–Os and Mo isotope systematics of black shales from the Middle Proterozoic Velkerri and Wollogorang formations, McArthur Basin, northern Australia. *Geochim. Cosmochim. Acta* **73**, 2534–2558 (2009).
55. G. M. Cox, A. Jarrett, D. Edwards, P. W. Crockford, G. P. Halverson, A. S. Collins, A. Poirier, Z. X. Li, Basin redox and primary productivity within the Mesoproterozoic Roper Seaway. *Chem. Geol.* **440**, 101–114 (2016).
56. D. Herwartz, A. Pack, T. J. Nagel, A CO_2 greenhouse efficiently warmed the early Earth and decreased seawater $^{18}O/^{16}O$ before the onset of plate tectonics. *Proc. Natl. Acad. Sci. U.S.A.* **118**, e2023617118 (2021).
57. P. A. E. P. von Strandmann, M. T. Jones, A. Joshua West, M. J. Murphy, E. W. Stokke, G. Tarbuck, D. J. Wilson, C. R. Pearce, D. N. Schmidt, Lithium isotope evidence for enhanced weathering and erosion during the Paleocene-Eocene Thermal Maximum. *Sci. Adv.* **7**, eabh4224 (2021).
58. S. Kender, K. Bogus, G. K. Pedersen, K. Dybkjær, T. A. Mather, E. Mariani, A. Ridgwell, J. B. Riding, T. Wagner, S. P. Hesselbo, M. J. Leng, Paleocene/Eocene carbon feedbacks triggered by volcanic activity. *Nat. Commun.* **12**, 5186 (2021).
59. P. A. E. P. von Strandmann, A. Desrochers, M. J. Murphy, A. J. Finlay, D. Selby, T. M. Lenton, Global climate stabilisation by chemical weathering during the Hirnantian glaciation. *Geochem. Perspect. Lett.* **3**, 230–237 (2017).
60. G.-Y. Wei, W. Wei, D. Wang, T. Li, X. Yang, G. A. Shields, F. Zhang, G. Li, T. Chen, T. Yang, H.-F. Ling, Enhanced chemical weathering triggered an expansion of euxinic seawater in the aftermath of the Sturtian glaciation. *Earth Planet. Sci. Lett.* **539**, 116244 (2020).
61. F. Zhang, M. Dellinger, R. G. Hilton, J. Yu, M. B. Allen, A. L. Densmore, H. Sun, Z. Jin, Hydrological control of river and seawater lithium isotopes. *Nat. Commun.* **13**, 3359 (2022).
62. P. A. E. Pogge von Strandmann, G. M. Henderson, The Li isotope response to mountain uplift. *Geology* **43**, 67–70 (2015).
63. T. Zhang, M. Li, X. Chen, T. Wang, Y. Shen, High atmospheric CO_2 levels in the early Mesoproterozoic estimated from paired carbon isotopic records from carbonates from North China. *Precambrian Res.* **380**, 106812 (2022).
64. L. R. Kump, S. L. Brantley, M. A. Arthur, Chemical weathering, atmospheric CO_2, and climate. *Annu. Rev. Earth Planet. Sci.* **28**, 611–667 (2000).
65. L. Sauzéat, R. L. Rudnick, C. Chauvel, M. Garçon, M. Tang, New perspectives on the Li isotopic composition of the upper continental crust and its weathering signature. *Earth Planet. Sci. Lett.* **428**, 181–192 (2015).

66. P. A. E. Pogge von Strandmann, H. C. Jenkyns, R. G. Woodfine, Lithium isotope evidence for enhanced weathering during Oceanic Anoxic Event 2. *Nat. Geosci.* **6**, 668–672 (2013).
67. M. Lechler, P. A. E. Pogge von Strandmann, H. C. Jenkyns, G. Prosser, M. Parente, Lithium-isotope evidence for enhanced silicate weathering during OAE 1a (Early Aptian Selli event). *Earth Planet. Sci. Lett.* **432**, 210–222 (2015).
68. A. J. Krause, A. Sluijs, R. van der Ploeg, T. M. Lenton, P. A. E. Pogge von Strandmann, Enhanced clay formation key in sustaining the Middle Eocene Climatic Optimum. *Nat. Geosci.* **16**, 730–738 (2023).
69. E. Andrews, P. A. E. Pogge von Strandmann, M. S. Fantle, Exploring the importance of authigenic clay formation in the global Li cycle. *Geochim. Cosmochim. Acta* **289**, 47–68 (2020).
70. J. Ma, R. Chadwick, K.-H. Seo, C. Dong, G. Huang, G. R. Foltz, J. H. Jiang, Responses of the tropical atmospheric circulation to climate change and connection to the hydrological cycle. *Annu. Rev. Earth Planet. Sci.* **46**, 549–580 (2018).
71. Y. Ye, X. Wang, H. Wang, H. Fan, Z. Chen, Q. Guo, Z. Wang, C. Wu, D. E. Canfield, S. Zhang, Phosphate oxygen isotopes constrain Mesoproterozoic marine temperatures and the paucity of phosphorite. *Chem. Geol.* **644**, 121831 (2024).
72. C. T. Reinhard, N. J. Planavsky, B. C. Gill, K. Ozaki, L. J. Robbins, T. W. Lyons, W. W. Fischer, C. Wang, D. B. Cole, K. O. Konhauser, Evolution of the global phosphorus cycle. *Nature* **541**, 386–389 (2017).
73. Y. Xiong, R. Guilbaud, C. L. Peacock, M. D. Krom, S. W. Poulton, Phosphorus controls on the formation of vivianite versus green rust under anoxic conditions. *Geochim. Cosmochim. Acta* **351**, 139–151 (2023).
74. A. Noffke, C. Hensen, S. Sommer, F. Scholz, L. Bohlen, T. Mosch, M. Graco, K. Wallmann, Benthic iron and phosphorus fluxes across the Peruvian oxygen minimum zone. *Limnol. Oceanogr.* **57**, 851–867 (2012).
75. R. N. Mitchell, U. Kirscher, M. Kunzmann, Y. Liu, G. M. Cox, Gulf of Nuna: Astrochronologic correlation of a Mesoproterozoic oceanic euxinic event. *Geology* **49**, 25–29 (2021).
76. M. J. Salisbury, J. R. Patton, A. J. R. Kent, C. Goldfinger, Y. Djadjadihardja, U. Hanifa, Deep-sea ash layers reveal evidence for large, late Pleistocene and Holocene explosive activity from Sumatra, Indonesia. *J. Volcanol. Geotherm. Res.* **231–232**, 61–71 (2012).
77. C. G. Newhall, S. Self, The volcanic explosivity index (VEI): An estimate of explosive magnitude for historical volcanism. *J. Geophys. Res. Oceans* **87**, 1231–1238 (1982).
78. Z. Huang, C. Yuan, X. Long, Y. Zhang, X. Ma, J. Soldner, L. Du, C. Shu, The cause for Nuna breakup in the Early to Middle Mesoproterozoic. *Precambrian Res.* **362**, 106287 (2021).
79. L. Xu, C. Luo, H. Wen, A revisited purification of Li for 'Na Breakthrough' and its isotopic determination by MC-ICP-MS. *Geostand. Geoanal. Res.* **44**, 201–214 (2020).

Acknowledgments: We thank the reviewers for constructive comments. We also acknowledge H. Wen and F. Li for the analysis of Li isotopes and D. E. Canfield for insightful discussion. **Funding:** This research was financially supported by the National Key Research and Development Program of China (2022YFF0800300 to X.W. and H.W., 2017YFC0603100 to S.Z. and H.W., and 2021YFA0718200 to J.H. and Y.Y.), the Strategic Priority Research Program of the Chinese Academy of Sciences (XDA14010101 to S.Z.), the National Natural Science Foundation of China (42225303 to X.W., 41973009 to W.Z., 41872125 to H.W., and 41530317 to S.Z.), and the ERC Consolidator (682760 CONTROLPASTCO2 to P.A.E.P.v.S.). **Author contributions:** S.Z. designed research; S.Z., H.W., X.W., W.Z., J.H., P.A.E.P.v.S., and Y.Y. performed research; S.Z., H.W., X.W., W.Z., J.H., P.A.E.P.v.S., Y.Y., M.S., Y. Liu, and Y. Lyu analyzed data; S.Z., H.W., X.W., W.Z., J.H., P.A.E.P.v.S., and Y.Y. wrote the paper. **Competing interests:** The authors declare that they have no competing interests. **Data and materials availability:** All data needed to evaluate the conclusions in the paper are present in the paper and/or the Supplementary Materials.

Submitted 30 August 2023
Accepted 26 February 2024
Published 29 March 2024
10.1126/sciadv.adk5991